System Performance Analysis of the Shoulder Elbow Perturbator

Van Zanten, Jonathan C.; Ter Welle, Karien; Haarman, Claudia J.W.; Schouten, Alfred C.; Van De Ruit, Mark; Mugge, Winfred; Stienen, Arno H.A.

DOI
10.1109/ICORR66766.2025.11063005

Publication date
2025

Document Version
Final published version

Published in
Proceedings of the International Conference on Rehabilitation Robotics, ICORR 2025

2025 International Conference On Rehabilitation Robotics (ICORR)
May 12-16, 2025. Chicago, IL, USA

System Performance Analysis of the Shoulder Elbow Perturbator

Jonathan C. van Zanten, Karien ter Welle, Claudia J.W. Haarman†, Alfred C. Schouten, Mark van de Ruit, Winfred Mugge, and Arno H.A. Stienen∗
Biomechanical Engineering, Delft University of Technology, The Netherlands

2025 International Conference On Rehabilitation Robotics (ICORR) | 979-8-3503-8068-2/25/$31.00 ©2025 IEEE | DOI: 10.1109/ICORR66766.2025.11063005

***Abstract*—To increase the quality of life of stroke patients, better diagnostics with the ability to identify the cause of motor impairment are needed. Robotic diagnostics increases the resolution of measurements, allows for tracking progress over a longer period, and can be used to evaluate new treatments. The Shoulder Elbow Perturbator (SEP) was developed to improve the diagnostics of post-stroke motor impairment. The SEP has already been tested on patients, showing promising results in identifying the cause of motor impairment, but no SEP system performance analysis has been published. To identify the joint properties of the elbow accurately, the SEP should have a bandwidth of at least 12 Hz. Furthermore, admittance and velocity control are required for various possible experimental tasks. This paper shows that the SEP performs adequately for the desired perturbations and experimental conditions for system identification of the human elbow. The SEP's performance is analysed with multisine signals to determine the bandwidth and endpoint dynamics. The velocity controller bandwidth is 50 Hz, and the admittance controller bandwidth is 65 Hz. Furthermore, the controller is stable. Thus, the SEP meets all the requirements and should be able to provide the desired perturbations and experimental conditions needed for system identification of the human elbow.**

***Index Terms*—Shoulder Elbow Perturbator, spasticity, rehabilitation robotics, stroke, (Haptic) Manipulator**

I. INTRODUCTION

Stroke survival rate has increased drastically over the last decades. Due to the increased survival rate and an ageing society, the prevalence of disability due to stroke increases [1]. Post-stroke disability greatly impacts the patient's ability to perform activities of daily living (ADL). Improving therapeutic interventions will reduce the patient's physical and mental burden, the physician's workload, and healthcare costs [2]. Stroke can cause a wide variety of motor impairments. However, diagnosing whether the cause of motor impairment is neural or non-neural is difficult as they present similar symptoms, such as paresis, synergy, co-contraction, spasticity, or viscoelastic tissue property alterations [3]. A diagnosis capable of differentiation of the causes of impairment is desired. Clinically, impairment is quantified using ordinal scales based on a physicians assessments of a patient's voluntary joint movement and resistance to passive movement. Examples are the Modified Ashworth Scale, the Modified Tardieu Scale or the Fugl-Meyer assessment [4]. The manual assessment of motor impairment after a stroke makes quantification and distinguishing between various causes of motor impairments challenging. Therefore, there is a need for objective measurements of motor impairment, with a particular focus on differentiating between non-neural and neural components [5].

Objective measurement, with the use of robotic diagnostics, increases the resolution of measurements, allows for tracking progress over a longer period, and can be used to evaluate new treatments [5]. The system identification technique, which uses robotic diagnostics, aims to objectively identify the mechanical properties of human limbs to determine the severity and cause of the patient's motor impairment [6].

There are several joint manipulators for assessing motor function for research purposes [7, 8]. The Shoulder Elbow Perturbator (SEP) (Hankamp Rehab, Enschede), shown in Fig. 1, was developed to improve post-stroke motor impairment diagnostics. The SEP has already been tested on patients, showing promising results in identifying the cause of motor impairment [6, 9]. However, the performance of the SEP, along with its control, has not been analysed in detail.

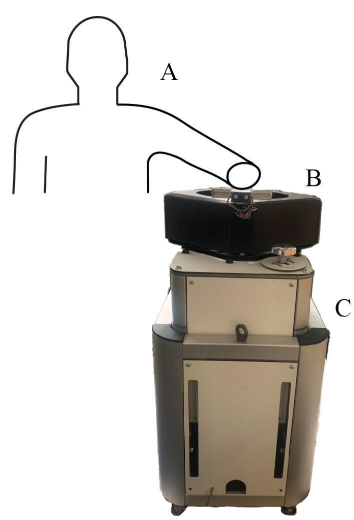

Fig. 1. The Shoulder Elbow Perturbator (SEP), with an illustration of a participant positioned in the device. The participant (A) is attached to the device with a clamp to the wrist on the ulnar and radial head. The table (B) can passively move in the vertical direction, allowing shoulder abduction and actively rotate the elbow in flexion and extension. The base (C) contains the motor and control detailed in Section II-B.

∗Jonathan C. van Zanten, Catherine S. ter Welle, Alfred C. Schouten, Mark van de Ruit, Winfred Mugge and Arno H.A. Stienen are with the Department of Biomechanical Engineering of Delft University of Technology (Netherlands). The email address for correspondence is J.C.vanZanten@tudelft.nl
†Claudia J.W. Haarman is with Hankamp Rehab, situated in Enschede.

TABLE I
HARDWARE SPECIFICATIONS OF THE SEP

Component	Hardware	Parameter	Specifications
Motor	Hiwin TMS3C	Encoder resolution	4,325,376 counts/revolution
Drive	Hiwin ED1-01	Device inertia	0.043 kg m^2
Transmission	Direct drive	Torque	60 Nm (180 Nm peak)
Force sensor & signal conditioner	Futek LCM200 AIAA100	Velocity Acceleration	1,800 deg/s 18,000 deg/s^2
Target PC	Lenovo Ideapad (Windows)	Range of motion (R1)	160 deg
Coupler & Terminals	Beckhoff EK1100 1x EL3102, 1x EL2002, 1x EL1202	Shoulder elevation range (D1)	20 cm

For this study, the controller performance of the SEP is optimized and the control is changed from only position control to admittance and velocity control. Admittance control is primarily used in combination with a position task. The advantage of using the position task with admittance control is that the control evokes consistent human motor control by interacting with adjustable virtual dynamics [10]. Velocity control is primarily used in combination with a force or relax task. Velocity control enables precise perturbation of the participant with the desired velocities, for example, to elicit stretch reflexes or quantify limb dynamics.

To be able to do experiments needed for system identification, the SEP should be able to perturb the arm with frequencies greater than or equal to three times the eigenfrequency of the elbow [7]. For the elbow joint, the eigenfrequency is approximately 3 Hz. For this paper, the requirement was set at four times the eigenfrequency, so the bandwidth of the SEP must be at least 12 Hz, with a stable controller. This paper shows the performance of the SEP for the desired perturbations and experimental conditions needed for system identification. The current paper shows the SEP's mechanical design, control scheme and analyses the overall system performance.

II. MECHANICAL DESIGN

A. Full Setup

A schematic representation of the mechanical setup of the SEP is shown in Fig. 2. The SEP can perturb the elbow in the horizontal plane with varying shoulder support. The elbow support is used to fixate the human elbow to the SEP by placing the elbow joint in line with the axis of rotation and clamping the wrist on the ulnar and radial head. The clamp's position can be adjusted to accommodate the patients' arm lengths. The sarrus linkage uses three parallel support beams to allow vertical movement of the elbow support while restricting horizontal movements. The linkage (3) connects the elbow support to the motor. This linkage is free to rotate whilst preserving vertical movement. The spring mechanism for the upward force provides an adjustable constant force over the range of motion. Table I presents the complete overview of the components used and their specifications [9]. Multiple safety layers, including mechanical end stops, electrical end stops, software end stops, and participant and operator emergency stops, ensure the safe operation of the SEP. The end stop location can be adjusted to ensure safety for participants with various passive ranges of motion.

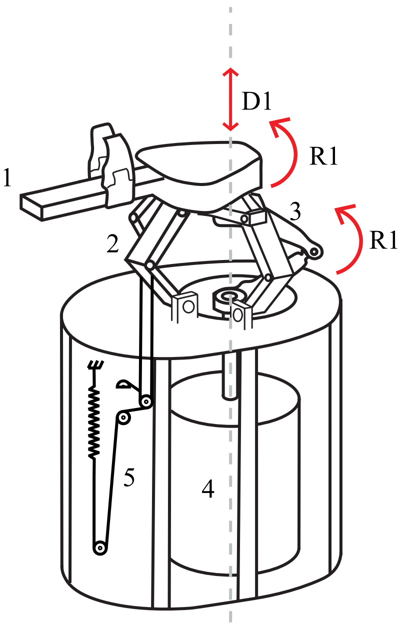

Fig. 2. Schematic representation of the SEP. The SEP contains the following parts: the elbow support (1), the Sarrus linkage, which houses the bearing for the rotation of parts 1 & 3, the linkage can not rotate or move horizontally (2), the motor-elbow support connection (3), the motor (4) and the spring mechanism exerting the constant upward force on the elbow support (5). R1 is the motor and elbow support rotation, of which the rotation axis is the grey dotted line. D1 is the possible passive vertical movement of the elbow support.

B. Hardware/Software architecture

The controller is implemented using Matlab Simulink 2024b. The Simulink model is converted to C-code and built onto the Beckhoff Twincat 3.1 software. Parameters can be controlled via Simulink in real-time. The motor driver is set to profile velocity mode. The motor driver is set to its tuneless function with the highest possible stiffness, so it follows the desired velocity to the tuneless function's maximum ability. The data used in the various control modes is transmitted back to the Simulink model from the motor and sensors. Fig. 3 shows the entire communication setup.

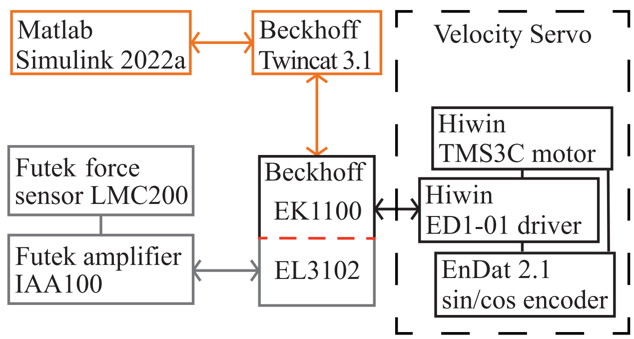

Fig. 3. Hardware/Software communication. The orange boxes represent the software running on a separate PC. The grey boxes are analogue sensors. The black boxes are digital hardware. The dotted red line represents the conversion of analogue to digital signals. The black dotted box shows the velocity servo hardware.

III. Control Scheme

The SEP has two modes of control: velocity control and admittance control. The following paragraphs explain both modes of control in detail.

A. Velocity control

In velocity control, the input is a velocity signal ($\dot{\theta}_d$) independent of the external loading in joint perturbations experiments caused by the arm and device dynamics. As mentioned in section II-B, the velocity servo is tuned to follow the input signal to its maximum ability. Thus, the motor produces the torque necessary to reach the desired velocity. The encoder measures the position (θ_m) and velocity ($\dot{\theta}_m$) of the motor used for analysis.

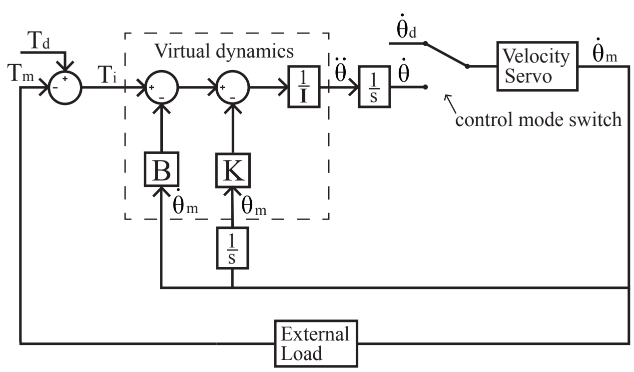

Fig. 4. Control diagram of the SEP for both modes of control. For admittance control, There is the measured torque (T_m), which is combined with a disturbance torque (T_d) to get the input for the virtual dynamics, referred to as the input torque (T_i). The virtual dynamics are the stiffness, damping and inertia, denoted with K, B and I, respectively. The output of the virtual dynamics is the desired acceleration, which is integrated to get the desired velocity. The desired velocity ($\dot{\theta}$) goes into the velocity servo, also shown in Fig. 3. The motor follows the desired velocity, resulting in a motor velocity ($\dot{\theta}_m$). The external load consists of the human and post-sensor device. The dynamics of the attached load (device + external load) on the motor create a resistance torque, the measured torque. For velocity control, there is a desired velocity ($\dot{\theta}_d$) as an input and a motor velocity ($\dot{\theta}_m$), which is the output of the driver.

B. Admittance control

In admittance control, the robotic controller's input is the external torque [11]. The controller has virtual dynamics that prescribe rotation, angular velocity, and angular acceleration in response to torque. Fig. 4 shows the admittance controller. The formula for the virtual dynamics is given in Equation 1

$$\ddot{\theta} I = T_d - T_m - B\dot{\theta}_m - K\theta_m \tag{1}$$

Where T_m is the measured torque. θ_m and $\dot{\theta}_m$ are measured the position and velocity, and T_d is the added disturbance torque for the performance analysis. Furthermore, the virtual dynamics are the stiffness, damping and inertia, denoted with K, B and I, respectively.

IV. Performance analysis

A. Perturbation signal for analysis

The perturbation signal is a multisine (i.e. a sum of sines) that excites the device over a wide frequency range of 0.1-100 Hz [12]. A wide range of perturbation frequencies helps to identify the frequency at which the servo velocity loop (H_{servo}) gain drops below -3 dB, indicating the controller bandwidth. The perturbation signal is scaled so the rotation remained within 6 degrees of the neutral position. For the experiments, the signal duration was 80 seconds. The signal was repeated four times in each trial, amounting to 320 s. Each trial was repeated five times to increase the accuracy of the performance analysis.

B. External load

The human arm introduces inertia, damping and stiffness as an external load. To ensure that the SEP functions with and without added external loads, external loading conditions were determined to mimic the extra load the human arm puts on the device. The human arm inertia was calculated by taking 2.5 kg as the weight of the arm [13], and 371 mm as the length of the forearm and hand [14] and the center of mass at 43% from its proximal end [13]. When calculating the inertia using these values, the arm inertia is $0.064\ \mathrm{kg\,m^2}$. The values are those of a large and heavy arm to get a high value for the inertia [13]. External damping is not introduced as elbow damping only makes a small contribution to the elbow joint impedance and is hard to realize. To mimic the added external stiffness of the human on the robot, two tension springs facing opposite directions are attached from the SEP to an external frame. Creating a bidirectional external stiffness of 0.84 $\mathrm{Nm/deg}$, which is in the order of magnitude of earlier identified elbow stiffness with the SEP [6]. The three external loading conditions are:

- No external load
- Added inertia (0.064 $\mathrm{kg\,m^2}$)
- Added inertia and rotational stiffness (0.064 $\mathrm{kg\,m^2}$ + 0.84 $\mathrm{Nm/deg}$)

C. Velocity control

The velocity servo's performance is tested in the velocity control mode, separately from the admittance control, to ensure that the admittance control's virtual dynamics do not suppress the high frequencies, which would create a less accurate estimate of the controllers' bandwidth.

D. Admittance control

The virtual dynamics were set to low impedance values that do not suppress too many high frequencies but maintain controller stability. The virtual dynamics were set to: $I = 0.01\ \mathrm{kg\,m^2}$, $B = 0.05\mathrm{Nm/s}$, $K = 0.5\ \mathrm{N/m}$.

E. Data processing

For the velocity control, the recorded signals during a trial were the numerically integrated input velocity (θ) and the motor position (θ_m). The frequency response function (FRF) ($\hat{H}_{velo}(f)$) is estimated in open-loop for the velocity control. For the estimation of FRFs, the power and cross-spectral densities were estimated using Welch averaging over four segments of 80 s. With these spectral densities ($\hat{S}_{output-input.}(f)$), the FRFs were estimated using the following equations:

$$\hat{H}_{velo}(f) = \frac{\hat{S}_{\theta_m\theta_d}(f)}{\hat{S}_{\theta_m\theta_m}(f)}. \tag{2}$$

Equation 3 calculates the coherence $\hat{\gamma}^2_{velo}(f)$ between the earlier defined variables (θ) and (θ_m). The coherence is a measure of the linearity and the signal-to-noise ratio. The coherence ranges from 0 to 1, with a value of 1 indicating the relationship between the input and output is linear and without noise. The coherence is estimated with the following equation:

$$\hat{\gamma}^2_{velo}(f) = \frac{|\hat{S}_{\theta_m\theta_d}(f)|^2}{\hat{S}_{\theta_m\theta_m}(f)\hat{S}_{\theta_d\theta_d}(f)}. \tag{3}$$

For the admittance control, the recorded signals during a trial were the disturbance torque (T_d), the measured torque (T_m), the input torque (T_i), the motor position (θ_m) and the numerically integrated input velocity (θ). Closed-loop estimators for the FRF were used to estimate the FRF for the virtual dynamics ($\hat{H}_{virt}(f)$), the velocity servo ($\hat{H}_{servo}(f)$), and the external load ($\hat{H}_{load}(f)$). These FRFs represent the virtual dynamics, velocity servo and external load block as defined in Fig. 4 respectively. For determining the controller stability, the open-loop FRF of the entire loop can be estimated ($\hat{H}_{loop}(f)$) with the earlier estimated FRFs. The FRFs were estimated using the following equations:

$$\hat{H}_{servo}(f) = \frac{\hat{S}_{\theta_m T_d}(f)}{\hat{S}_{\theta T_d}(f)}, \tag{4}$$

$$\hat{H}_{(f)} = \frac{\hat{S}_{\theta T_d}(f)}{\hat{S}_{T_i T_d}(f)}, \tag{5}$$

$$\hat{H}_{load}(f) = \frac{\hat{S}_{\theta_m T_d}(f)}{\hat{S}_{T_d T_m}(f)}, \tag{6}$$

$$\hat{H}_{loop}(f) = \hat{H}_{load}(f)\hat{H}_{servo}(f)\hat{H}_{virt}(f). \tag{7}$$

Finally, in addition to the FRF, the coherence $\hat{\gamma}^2_{adm}(f)$ between the disturbance torque and the output position was estimated.

$$\hat{\gamma}^2_{adm}(f) = \frac{|\hat{S}_{\theta T_d}(f)|^2}{\hat{S}_{\theta\theta}(f)\hat{S}_{T_d T_d}(f)}. \tag{8}$$

V. Results

A. Velocity control performance

Fig. 5 shows half a second of the desired- and output velocities for each loading condition, with the controller set to velocity control.

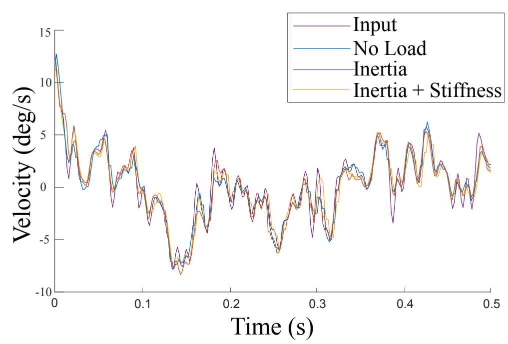

Fig. 5. Half a second of the desired- and motor velocity for each loading condition. The figure shows that the motor velocities of all external loading conditions approximate the desired velocity in this short time window.

The top two panels of Fig. 6 show the magnitude and phase of the velocity control FRF function ($\hat{H}_{velo}(f)$). The bandwidth of the velocity controller is 50 Hz. The bottom panel of Fig. 6 shows that the velocity controllers coherence $\hat{\gamma}^2_{velo}(f)$, which shows a linear behaviour throughout the required bandwidth.

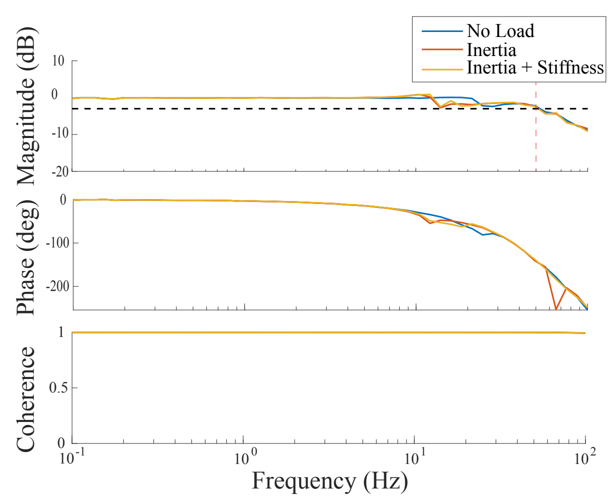

Fig. 6. The top two panels of the figure show the magnitude and phase of the FRF of the velocity controller ($\hat{H}_{velo}(f)$). The magnitude remains on the 0dB line up to 13 Hz and crosses the -3dB line at 50 Hz, shown with the red dotted line; the bottom panel shows the coherence between the actual and desired velocity $\hat{\gamma}^2_{velo}(f)$, which remains above 0.99 up to 100 Hz

B. Admittance control performance

Fig. 7 shows the FRF of the velocity servo of the admittance controller ($\hat{H}_{servo}(f)$) for the three loading conditions. The bandwidth of the ($\hat{H}_{servo}(f)$) of the admittance controller is 65 Hz when only external inertia is added and 76 Hz for the other external loading conditions.

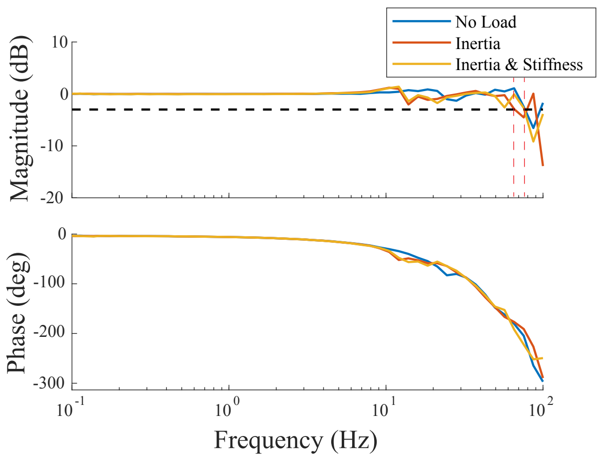

Fig. 7. Magnitude and phase plot of the FRF of the velocity servo of the admittance controller. The magnitude remains 0 dB for frequencies up to 24 Hz. The magnitude crosses the -3dB line at 65 Hz when only external inertia is added and at 76 Hz for the other external loading conditions. The magnitude crossing is shown with a red dotted line. The phase lag becomes noticeable beyond 10 Hz.

The top two panels of Fig. 8 show the magnitude and phase plots for $\hat{H}_{load}(f)$. For the frequencies between 0.3 Hz and 10 Hz the magnitude and phase plot clearly shows the dynamics of a system with only mass for the blue and orange lines and shows the dynamics of a system with mass and stiffness for the yellow line. The bottom panel of Fig. 8 shows the coherence $\hat{\gamma}^2_{adm}(f)$; the drop after 50 Hz indicates the noise becomes more prevalent than the signal.

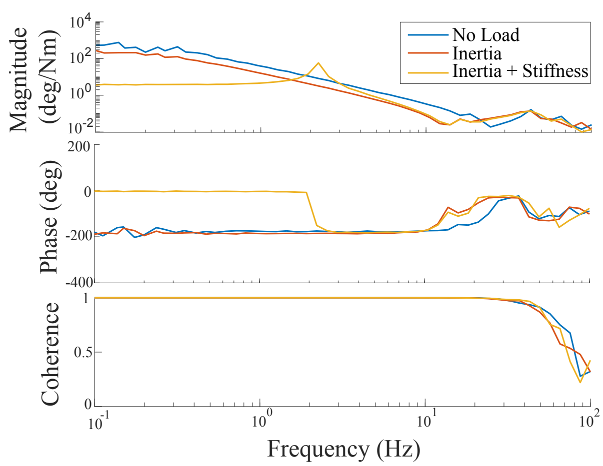

Fig. 8. The top two panels show the magnitude and phase plot of the external load $\hat{H}_{load}(f)$. The bottom panel shows the coherence $\hat{\gamma}^2_{adm}(f)$. The coherence drops below 0.9 at a frequency of 50 Hz.

From the Nyquist plot of the open-loop admittance control loop gain, the stability of a controller can be determined by checking if the (-1,0) point is encircled. The Nyquist plot of this controller showed no encirclement, so the control is stable.

VI. Discussion

This paper analysed whether the SEP performs adequately for the desired perturbations and experimental conditions needed for system identification with a stable controller. The bandwidth of the velocity servo in the admittance control mode is 65 Hz, while the same velocity servo in the velocity control mode has a bandwidth of 50 Hz. Both bandwidths are at least four times higher than the required bandwidth, so this requirement is met. The difference in bandwidth between the control modes could come from the fact that the virtual dynamics of the admittance controller suppress high frequencies, making the performance needed for the admittance controller to reach a specific bandwidth lower, explaining the higher bandwidth. For both controllers, the magnitude remains 0 up to at least 13 Hz, meaning the controller exactly follows the input. The phases of both controllers lag after a frequency of 10 Hz. Phase lag in the control system means a delay between the system's input and output, which can lead to instability. Yet, with the present phase lag, the controller is still stable. The phase lag can be reduced by increasing the sampling time of the controllers. The performance of the SEP can be compared to other robots used to identify human limb joint parameters. Schouten et al. [7] developed a robot to analyse the wrist joint. Here, the bandwidth needed for wrist parameter identification is 50Hz, which is also their controller's reached bandwidth. Another example of a robot identifying joint parameters is the ACT4D, which analyses the elbow joint. Stienen et al. [8] show a FRF that has a magnitude of 1(-) up to 40 Hz. However, their FRF does not go below 0.7 (being the -3dB line). Meaning the bandwidth of their controller is higher than 100 Hz. The performance of the shoulder elbow perturbator is somewhat lower but still meets the set requirements.

A. Limitations

One limitation is the low input velocity. A higher power of the desired velocity input asks more of the velocity servo and motor hardware, thus possibly decreasing bandwidth. This effect is also observed in the previously discussed difference between the bandwidth of the velocity and admittance control. As the current identified bandwidth is four times higher than the needed bandwidth, it is likely that the required 12 Hz bandwidth is still met with a higher input power. To ensure this is the case, further testing should be performed. A current limitation is that the data processing and collection are done at 500 Hz. A higher frequency may be needed for better performance and future controller extensions. A higher frequency will also reduce the phase lag observed in the results. Additionally, the experiment can be followed up by conducting tests on human subjects, providing us with further insights into the SEP's comfort and usability, alongside the performance of the new controller of the SEP.

VII. Conclusion

This paper shows the performance of the SEP with velocity and admittance control. The bandwidth needed for system identification of the elbow must be higher than 12 Hz for both control modes. The bandwidth of the velocity servo of the admittance control mode is 65 Hz. The velocity controller has a bandwidth of 50 Hz. Both bandwidths are at least four times higher than the set requirement. Furthermore, the controller is stable. Lastly, the frequency response function of the external load clearly shows the dynamics introduced to the system, laying the foundation for further research. These results show that the SEP meets all the requirements, meaning it should be able to provide the desired perturbations and experimental conditions needed for system identification of the human elbow.

VIII. Acknowledgments

The authors wish to express their sincere gratitude for the invaluable support and collaboration of their partners: Hankamp Rehab, Amsterdam University Medical Center, Amsterdam Movement Sciences, Erasmus Medical Center, and Rijndam Revalidatie.

References

[1] C. O. Johnson, M. Nguyen, and G. A. et al. Roth. "Global, regional, and national burden of stroke, 1990–2016: A systematic analysis for the Global Burden of Disease Study 2016". In: *The Lancet Neurology* 18.5 (May 2019), pp. 439–458. ISSN: 1474-4422. DOI: 10.1016/S1474-4422(19)30034-1.

[2] H. P. Neil. "Stroke rehabilitation". In: *Critical Care Nursing Clinics of North America* 35.1 (Mar. 2023), pp. 95–99. ISSN: 0899-5885. DOI: 10.1016/j.cnc.2022.11.002.

[3] P. Raghavan. "Upper limb motor impairment after stroke". In: *Physical Medicine and Rehabilitation Clinics of North America* 26.4 (Nov. 2015), pp. 599–610. ISSN: 1047-9651. DOI: 10.1016/j.pmr.2015.06.008.

[4] A. D. Pandyan, G. R. Johnson, and C. I. M. et al. Price. "A review of the properties and limitations of the Ashworth and modified Ashworth scales as measures of spasticity". In: *Clinical Rehabilitation* 13.5 (Oct. 1999), pp. 373–383. ISSN: 0269-2155. DOI: 10.1191/026921599677595404.

[5] H. J. M. van der Krogt et al. "The gap between clinical gaze and systematic assessment of movement disorders after stroke". In: *Journal of NeuroEngineering and Rehabilitation* 9 (Aug. 2012), p. 61. ISSN: 1743-0003. DOI: 10.1186/1743-0003-9-61.

[6] M. van de Ruit et al. "System identification: A feasible, reliable, and valid way to quantify upper limb motor impairments". In: *Journal of NeuroEngineering and Rehabilitation* 20.1 (May 2023), p. 67. ISSN: 1743-0003. DOI: 10.1186/s12984-023-01192-x.

[7] A. C. Schouten et al. "Design of a torque-controlled manipulator to analyse the admittance of the wrist joint". In: *Journal of Neuroscience Methods* 154 (June 2006), pp. 134–141. ISSN: 0165-0270. DOI: 10.1016/j.jneumeth.2005.12.001.

[8] A. H. A. Stienen et al. "The ACT-4D: A novel rehabilitation robot for the quantification of upper limb motor impairments following brain injury". In: *2011 IEEE International Conference on Rehabilitation Robotics*. IEEE, June 2011, pp. 1–6. ISBN: 978-1-4244-9862-8. DOI: 10.1109/ICORR.2011.5975460.

[9] L. L. van der Velden et al. "Development of a single device to quantify motor impairments of the elbow: Proof of concept". In: *Journal of NeuroEngineering and Rehabilitation* 19.1 (Dec. 2022), p. 77. ISSN: 1743-0003. DOI: 10.1186/s12984-022-01050-2.

[10] W. Mugge et al. "A rigorous model of reflex function indicates that position and force feedback are flexibly tuned to position and force tasks". In: *Experimental Brain Research* 200 (Jan. 2010), pp. 325–340. ISSN: 0014-4819. DOI: 10.1007/s00221-009-1985-0.

[11] A. Q. L. Keemink, H. van der Kooij, and A. H. A. Stienen. "Admittance control for physical human–robot interaction". In: *The International Journal of Robotics Research* 37 (Sept. 2018), pp. 1421–1444. ISSN: 0278-3649. DOI: 10.1177/0278364918768950.

[12] R. Pintelon and J. Schoukens. *System Identification*. John Wiley & Sons, Mar. 2012.

[13] S. Plagenhoef, F. G. Evans, and T. Abdelnour. "Anatomical data for analyzing human motion". In: *Research Quarterly for Exercise and Sport* 54 (1983), pp. 169–178. URL: https://api.semanticscholar.org/CorpusID:143387656.

[14] *DINED*. 2004. URL: https://dined.nl/en/database/tool.